PHYSICAL REVIEW D **74,** 104027 (2006)

Nonuniform black strings in various dimensions

Evgeny Sorkin*

Department of Physics and Astronomy, University of British Columbia, 6224 Agricultural Road, Vancouver, V6G 1Z1, Canada

(Received 8 September 2006; published 22 November 2006)

The nonuniform black-strings branch, which emerges from the critical Gregory-Laflamme string, is numerically constructed in dimensions $6 \leq D \leq 11$ and extended into the strongly nonlinear regime. All the solutions are more massive and less entropic than the marginal string. We find the asymptotic values of the mass, the entropy and other physical variables in the limit of large horizon deformations. By explicit metric comparison we verify that the local geometry around the waist of our most nonuniform solutions is conelike with less than 10% deviation. We find evidence that in this regime the characteristic length scale has a power-law dependence on a parameter along the branch of the solutions, and estimate the critical exponent.

DOI: 10.1103/PhysRevD.74.104027 PACS numbers: 04.50.+h, 04.70.Bw, 04.25.Dm

I. INTRODUCTION AND SUMMARY

The surprising discovery of Gregory and Laflamme (GL) [1] that below certain mass the uniform black strings, existing in the backgrounds with compact extra dimensions, are perturbatively unstable created considerable excitement. It initiated intensive research aimed to understand the consequences of this instability and to figure out its endpoint. In this regard, some progress has been made in the numerical simulations of the decaying string [2]. Yet, the endpoint remains elusive as the simulations crash (due to numerical problems) when the spacetime is still highly dynamical and far from settling down to the static solution. A different program [3] to determine the endstate proposes to find a phase diagram accommodating all possible static solutions. The hope is that in principle the endstate can be inferred from the diagram since by definition it is a static solution. This research has recently culminated in the reviews [4,5].

A proposed phase diagram is portrayed in Fig. 1. The vertical axis shows the dimensionless mass density while the horizontal axis is related to the scalar charge. The branches of solutions represented by solid lines are presumably stable and the dashed lines indicate unstable solutions. The diagram has several remarkable features: (1) The merger point where the black-hole branch meets the black-string branch and where the horizon topology changes. (2) A critical dimension $D_{\text{2D order}} = 13$ above which the order of the phase transition changes from the first to the second [6] and where the emergent branch of nonuniform solutions becomes (thermodynamically) stable [7]. According to the diagram, the endpoint of the GL instability depends on the dimension and it is either a caged black hole in $D \leq 13$ or a nonuniform black string otherwise. For now, only certain parts of the diagram in certain dimensions were verified by analytical/numerical constructions. This is described next.

*Electronic address: evgeny@physics.ubc.ca

The black-hole branch has been constructed numerically in five [8,9] and six [9,10] dimensions. In particular, it has been shown to approach the merger point, where the north and the south poles of the caged black hole are expected to intersect across the compact dimension [9]. In other dimensions only the beginning of the BHs branch was constructed perturbatively from the Schwarzschild-Tangherlini [11] solution in [12–15] and numerically in [16]. The branch of the NUBS was found perturbatively from the critical GL string in five [17], six [18] and in other, up to 16, dimensions [6]. In six [18] and in five [19] dimensions the branch was numerically extended into nonlinear regime, where it was shown to behave in accordance with diagram 1(a).

In this paper we aim to construct the NUBS branch in higher dimensions and to extend it beyond linear perturbations into the strongly nonuniform regime. To define the

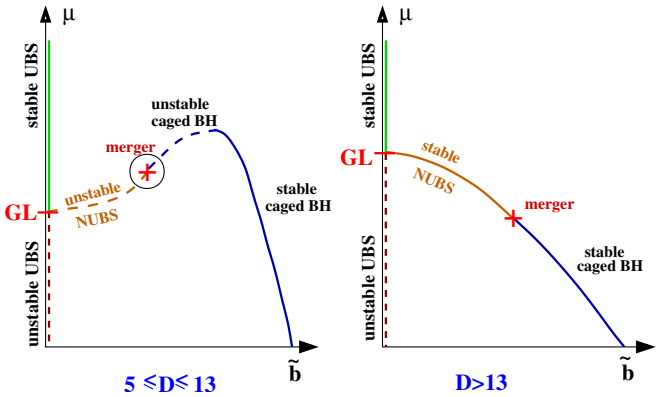

FIG. 1 (color online). A suggested phase diagram. The vertical axis is the dimensionless mass density and the horizontal axis is related to the scalar charge. Shown is the GL point where the uniform string becomes marginally unstable and from which a new branch of nonuniform strings emerges. This branch extends until it meets the caged black-hole branch at the ''merger point.'' In $D > 13$ the NUBSs branch is less massive than the critical string indicating that the order of the phase transition, triggered by appearance of the GL-mode, changes from first to second.

''nonlinear,'' ''strongly nonuniform'' regime we use a simple geometrical measure of the horizon deformation [17],

$$\lambda \equiv \frac{1}{2}\left(\frac{R_{\max}}{R_{\min}} - 1\right), \tag{1}$$

where $R_{\min}/R_{\max}$ are the minimal/maximal areal radii of $z = \text{const}$ sections of the horizon. $\lambda = 0$ for uniform strings and $\lambda \to \infty$ at the pinch-off.[1] It turns out that while at pinch-off, $R_{\min} \to 0$, many other thermodynamical and geometrical quantities, describing the NUBSs, asymptote to finite values. This fact suggests a natural definition of the strongly nonlinear regime as a situation when these variables are close to saturation.[2]

Recently, intriguing proposals regarding the local geometry near the ''waist'' of the extremely nonuniform strings have been put forward by Kol [3,20]. Specifically, in [3] Kol advocates that locally the merger spacetime is conelike, and moreover in $D \leq 10$ the local slightly off-merger metric and its functions have power-law dependence on parametric distance from the critical (merger) cone. In other words, if p is a parametrization of the static NUBSs branch, such that $p*$ corresponds to the merger, than quantities with the length dimensions are conjectured to scale as

$$\log(\ell) = \gamma \log(p - p*) + \phi[\gamma \log(p - p*) + \text{const}] + \text{const}, \tag{2}$$

where ϕ is a periodic function.[3] Namely the leading behavior is a power-law with an exponent γ; and this is dressed with periodic ''wiggles.''

Unfortunately, the data available in literature provides only limited insights on what happens at the merger since neither along NUBS nor along the BH branches is the merger point approached close enough. Still, some evidence in favor of the local cone geometry was reported in [25]. The scaling (2) has not been tested so far.

In this paper, we partially close the gaps. We use numerical techniques to find fully nonlinear branches of NUBSs in dimensions from six to eleven and confirm that these are in accordance with diagram 1(a). In dimensions 6, 7, 8, and 9 we are able to extend the NUBSs branch into the deeply nonlinear regime. In this range of the dimensions we find the limiting values of the thermodynamic and geometric variables, these are listed in Table I. Furthermore, since our method allows approaching the merger very closely, we compare the local near waist geometry with a cone. This is explicitly done in 6D where we have our most nonuniform solutions with the highest resolution. We find that the metrics agree well and the agreement improves with growing λ. For our most nonuniform solution the discrepancy between the near-waist metric and the cone does not exceed 10%.

Next, we verify the scaling (2) and find evidence for the power-law. We extract the approximate critical exponents and list them in Table II. However, the wiggles are not seen for our nonuniform solutions. We believe that in order to actually test for the presence of wiggles, one must have solutions spanning over several orders of magnitude in λ. Currently, this challenging task stands beyond the capabilities of our numerical experiments.

In the next section we describe the setup and derive the field equations and the boundary conditions. We define the physical variables and describe how the cone and the scaling (2) are tested. In Sec. III we elaborate on our numerical method. In Sec. IV we describe the solutions and their properties and discuss them in Sec. V. Various technical details are found in the appendices.

II. STATIC BLACK STRINGS

We consider D-dimensional background of the form $\mathbb{R}^{D-2,1} \times \mathbf{S}^1$, that has one spatial dimension, z, compactified on a circle of length L, $z \sim z + L$. We are interested in static black objects, which are spherically symmetric in the extended dimensions. The simplest such a solution is the uniform black string whose metric in Schwarzschild coordinates is given by

$$\begin{aligned} ds_c^2 &= ds_{\text{Schw}_d}^2 + dz^2, \\ ds_{\text{Schw}_d}^2 &= -f(\rho)dt^2 + f(\rho)^{-1}d\rho^2 + \rho^2 d\Omega_{d-2}^2, \end{aligned} \tag{3}$$

where $f(\rho) = 1 - (\rho_0/\rho)^{d-3}$, ρ_0 designates the horizon location and $d\Omega_{d-2}^2$ is the metric on a unit sphere $\mathbf{S}^{d-2}$. Gregory and Laflamme showed that this string is unstable below certain mass [1]. Here, we construct the branch of static nonuniform black strings that emanates from the GL-point.

The most general metric describing the black strings can be written as

$$ds^2 = -e^{2\hat{A}}dt^2 + d\sigma(r,z)^2 + e^{2\hat{C}}d\Omega_{D-3}^2, \tag{4}$$

where $\hat{A}$ and $\hat{C}$ are functions of r and z, $d\sigma(r,z)^2$ is a two-dimensional metric in the (r,z) plane. The horizon is located where $\exp(\hat{A}) = 0$. A convenient ansatz that we employ in this paper[4] uses ''conformal'' coordinates in which

$$ds^2 = -f(\rho(r))e^{2A} + e^{2B}(dr^2 + dz^2) + \rho(r)^2 e^{2C} d\Omega_{D-3}^2. \tag{5}$$

[1] Apparently, $R_{\max}$ remains finite in this limit.

[2] The saturation is best noted using λ, since in λ the measurables approach their limiting values roughly exponentially.

[3] This sort of behavior is known to appear [21,22] in the near-critical collapse of a scalar field [23] (see [24] for a D-dimensional version). Indeed, there are speculations [20] that the merger cone might be related to the critical collapse by a double analytic continuation and change of the boundary conditions.

[4] We found that the explicit separation of the UBS background is essential for stability of our numerical scheme.

When $A = B = C = 0$ we reproduce the UBS solution in conformal coordinates (the transformation $\rho \mapsto r$ from Schwarzschild to the conformal coordinates is described in appendix A.) The horizon is located at the radius r_0, where $f(r_0) = 0$. Without loss of generality we assume $r_0 = 0$.

A. Equations and boundary conditions

In order to find the black strings we solve the Einstein equations, $R_{ab} = 0$, that in our coordinates (5) split into three elliptic equations

$$\begin{aligned}
&\triangle A + (\partial_r A)^2 + (\partial_z A)^2 + (D-3)(\partial_r A \partial_r C + \partial_z A \partial_z C) + \frac{D-4}{2\rho\sqrt{f}}(2\partial_r A + (D-3)\partial_r C) \\
&\qquad + \frac{\sqrt{f}}{2\rho}(2\partial_r A - (D-3)(D-4)\partial_r C) = 0, \\
&\triangle B - \frac{D-3}{2}(2\partial_r A + (D-4)\partial_r C)\partial_r C - \frac{D-3}{2}(2\partial_z A + (D-4)\partial_z C)\partial_z C - \frac{(D-3)(D-4)}{2\rho\sqrt{f}}\partial_r C \\
&\qquad - \frac{(D-3)\sqrt{f}}{2\rho}(2\partial_r A + (D-4)\partial_r C) - \frac{(D-3)(D-4)}{2}\frac{1-e^{2B-2C}}{\rho^2} = 0, \\
&\triangle C + (\partial_r A + (D-3)\partial_r C)\partial_r C + (\partial_z A + (D-3)\partial_z C)\partial_z C + \frac{(D-4)}{2\rho\sqrt{f}}\partial_r C + \frac{\sqrt{f}}{2\rho}(2\partial_r A + (3D-8)\partial_r C) \\
&\qquad + (D-4)\frac{1-e^{2B-2C}}{\rho^2} = 0, \qquad (6)
\end{aligned}$$

where $\triangle \equiv \partial_z^2 + \partial_r^2$, and two hyperbolic constraints

$$\begin{aligned}
&G^r_z\colon\ \partial_{rz}A + (D-3)\partial_{rz}C - \partial_r A(\partial_z B - \partial_z A) - (D-3)\partial_r C(\partial_z B - \partial_z C) - \partial_r B(\partial_z A + (D-3)\partial_z C) \\
&\qquad + \frac{(D-4)(1-f)}{2\sqrt{f}\rho}(\partial_z A - \partial_z B) - \frac{(D-3)\sqrt{f}}{\rho}(\partial_z B - \partial_z C) = 0, \\
&G^z_z - G^r_r\colon\ \partial_z^2 A - \partial_r^2 A + (D-3)(\partial_z^2 C - \partial_r^2 C) + (\partial_z A)^2 - (\partial_r A)^2 + (D-3)[(\partial_z C)^2 - (\partial_r C)^2] - 2\partial_z A\partial_z B + 2\partial_r A\partial_r B \\
&\quad - 2(D-3)(\partial_z B\partial_z C - \partial_r B\partial_r C) - \frac{D-4}{\rho\sqrt{f}}(\partial_r A - \partial_r B) + \frac{\sqrt{f}}{\rho}[(D-4)\partial_r A + (D-2)\partial_r B - 2(D-3)\partial_r C] = 0. \qquad (7)
\end{aligned}$$

As first observed by Wiseman [26], the Bianchi identities, $G^b_{a;b} = 0$, imply that the constraints satisfy Cauchy-Riemann relations,

$$\partial_z \mathcal{U} + \partial_r \mathcal{V} = 0, \qquad \partial_r \mathcal{U} - \partial_z \mathcal{V} = 0, \qquad \mathcal{U} \equiv \sqrt{-g}G^z_r, \qquad \mathcal{V} \equiv \tfrac{1}{2}\sqrt{-g}(G^r_r - G^z_z). \qquad (8)$$

This in turn means that each one of $\mathcal{U}$ and $\mathcal{V}$ separately satisfy the Laplace equation. Hence, the "constraint rule" follows: provided one of the constraints vanishes along the boundary of the domain and the second one is zero at a single point of the boundary—both constraints are guaranteed to vanish inside the domain [26].

The elliptic Eqs. (6) are solved outside of the horizon. The periodicity in z and the reflection[5] symmetry at $z = 0$ suggest the sufficient domain of integration $\{(r, z)\colon 0 \le z \le L/2, r \ge 0\}$.

The equations are subject to boundary conditions (b.c.) The reflection symmetry at $z = 0$ and the periodicity at $z = L/2$ are translated into

$$\partial_z \Psi|_{z=0} = \partial_z \Psi|_{z=L/2} = 0 \quad \text{for} \quad \Psi = A, B, C. \qquad (9)$$

A regularity of (6) at the horizon supplies two conditions

$$\partial_r A|_{r=0} = \partial_r C|_{r=0} = 0. \qquad (10)$$

However, we need 3 b.c. for our three fields. The missing condition is obtained from the "constraint rule", following which we impose $\mathcal{U} = 0$ along all boundaries. The constraint is automatically satisfied along $z = 0$ and $z = L/2$

[5] An appearance of the GL zero-mode spontaneously breaks the translational invariance along z. The remaining symmetry to the translation by half a period implies that the branch of NUBS solutions that emerges from the GL-point has reflection symmetry about $z = 0$.

due to (9), and it vanishes exponentially at large r (as does any z-dependence in a Kaluza-Klein background). A regularity of $\mathcal{U}$ at the horizon yields

$$(\partial_z B - \partial_z A)|_{r=0} = 0, \tag{11}$$

and implies that the surface gravity is constant along static horizon. Integrating (11) from $z = L/2$ we obtain a Direchlet boundary condition for B,

$$B(0, z) = B|_{z=L/2} + A(0, z) - A|_{z=L/2}. \tag{12}$$

The integration constant $B_0 \equiv B|_{z=L/2}$ is freely specifiable; once it is chosen the NUBS solution is unique for a given L. $B_0 = 0$ corresponds to a unform string, a positive B_0 yields certain nonuniform string solution.[6]

Asymptotically we require that the spacetime is cylindrically-flat, $A = B = C = 0$. The leading fall-off of the fields in this region is [27]

$$A \simeq \frac{a}{r^{D-4}}; \qquad B \simeq \frac{b}{r^{D-4}}; \qquad C \simeq \frac{c\log(r)}{r} \quad \text{for } D = 5,$$
$$C \simeq \frac{c}{r} \quad \text{for } D > 5. \tag{13}$$

This form is useful in numerical implementations whenever the asymptotic boundary is placed at a finite r.

Following the constraint rule and imposing $\mathcal{V} = 0$ at the asymptotic boundary will relate the asymptotic constants[7] in (13). However, in our numerical method which has the outer boundary at a finite r_a, we could get better overall accuracy by simply enforcing the falloffs (13) along r_a. The constraints are verified in Appendix B.

B. Charges and geometry

Thermodynamic properties of the solutions are determined by the asymptotic charges—the mass and the tension, and by the horizon measurables—the surface gravity and the horizon area. The variables are related by the generalized Smarr's formula. The geometry of the black-strings is conveniently visualized by embedding their horizon into flat space and by examining the proper length of the compact circle along $r = \text{const}$ slices.

1. Asymptotics and charges

The charges are related to the asymptotic constants (13) by [27,28]

$$\begin{bmatrix} m \\ \tau L \end{bmatrix} = \frac{\Omega_{D-3}}{8\pi}\begin{bmatrix} D-3 & -1 \\ 1 & -(D-3) \end{bmatrix}\begin{bmatrix} a + \frac{1}{2}\rho_0^{D-4} \\ b \end{bmatrix}, \tag{14}$$

where $\Omega_{D-1} \equiv D\pi^{D/2}/\Gamma(D/2+1)$ is the surface area of a unit $\mathbf{S}^{D-1}$ sphere, and $\rho_0^{D-4}/2$ originates from the background $f(\rho(r))$, see (5). (We set below $\rho_0 = 1$). For convenience we use the "asymptotic adapted" units in which the d-dimensional Newton's constant $G_d = G_D/L = 1$.

The dimensionless charges, defined with respect to the critical uniform black string's values (which can be read from (14) after setting $a = b = 0$), are

$$\hat{m} \equiv m/m_c = 1 + 2a - 2b/(D-3),$$
$$\hat{\tau} \equiv \tau/\tau_c = 1 + 2a - 2b(D-3). \tag{15}$$

Notice the factor $D-3$ that in higher dimensions increases the significance of b in the tension computation and suppresses it relatively to a in the mass calculation.

One can also define the relative tension, $n \equiv \tau L/m$. Normalizing with respect to $n_c = 1/(D-3)$ one has

$$\hat{n} \equiv n/n_c = \frac{1 + 2a - 2b(D-3)}{(D-3)(1+2a) - 2b}. \tag{16}$$

2. Horizon variables

The normalized temperature (or surface gravity) of the horizon reads

$$\hat{T} = \hat{\kappa} \equiv \kappa/\kappa_c = e^{A-B}|_{r=0}, \tag{17}$$

where $T \equiv \kappa/(2\pi)$ and $\kappa_c = \frac{1}{2}f'(\rho_0) = (D-4)/2$. The normalized horizon area is given by

$$\hat{A} \equiv A/A_c = \frac{1}{L}\int_0^L e^{B+(D-3)C}|_{r=0}dz, \tag{18}$$

where $A_c = L\Omega_{D-3}$ is the surface area of the critical string.

The horizon measurables are related to the asymptotic charges by the generalized Smarr's formula [27,28],

$$(D-3)m = (D-2)ST + \tau L, \tag{19}$$

where $S \equiv A/4G_D$ is the Bekenstein-Hawking entropy.

The first law of thermodynamics relates variations of the thermodynamic variables. If the asymptotic length of the compact circle is kept fixed (as in our case), the first law reduces to

$$dm = TdS \Rightarrow d\hat{m} = \hat{T}d\hat{S}\frac{T_c S_c}{m_c} \Rightarrow d\hat{m} = \hat{T}d\hat{S}\frac{D-4}{D-3}. \tag{20}$$

3. Geometry

We examine the black string's geometry by embedding the $r = \text{const}$ hypersurfaces into flat space,

[6] An alternative way to specify the integration constant is to fix the surface gravity κ. This determines B along the horizon as $B = A - \log\kappa$. We checked that both approaches produce comparable results. In either case, there is only one constant (either B_0 or κ) that has to be chosen. We fix B_0 and in this case the thermodynamical κ becomes a derived quantity.

[7] To this end, one must also include the subleading term in the expansion of C, that for $D > 5$ is $\tilde{c}/r^2$.

$$ds^2_{\rm flat} = dZ_e^2 + R_e^2 d\Omega^2_{D-3}, \qquad dZ_e = e^{B(r,z)}dz, \qquad R_e = e^{C(r,z)}\rho(r). \tag{21}$$

The dimensionless proper length of the compact circle along an $r = \text{const}$ hypersurface is given by

$$\hat{L}_{\rm prop}(r) \equiv \frac{1}{L}\int dZ_e(r) = \frac{1}{L}\int_0^L e^{B(r,z)}dz. \tag{22}$$

In particular, the dimensionless proper length of the horizon is $\hat{L}_{\rm hor} = \hat{L}_{\rm prop}(0)$. The horizon's areal radius, $R_e(z) = e^{C(0,z)}$, is not constant along the z-direction.

C. Near the merger point

For progressively nonuniform strings the minimal areal radius of the horizon, $R_{\rm min}$, is steadily shrinking. Kol [3] argues that in the regime when $R_{\rm min} \to 0$ the local geometry in vicinity of the waist becomes conelike, (see also additional arguments in recent [29]). Moreover, there is the power-low scaling (2), which in $D < 10$ is dressed with periodic wiggles [20].

A direct comparison of the 6D solutions of [18] with the cone metric was already carried in [25], where in spite of low numerical resolution authors indeed found some evidence in favor of the cone geometry. In this paper, by performing similar comparison, we provide additional, more quantitative support to the cone conjecture. In addition, we test the scaling (2) and observe the power-law, but no wiggles in any dimensions.

It is convenient to reproduce here the relevant formulae from [3,25] adopting them to our coordinates (5). The comparison of the string's spacetime with the cone is done in Euclidean signature. The transformation is achieved by defining $t_E \equiv it$ which takes the metric (5) to

$$ds^2 = f(\rho(r))e^{2A}dt_E^2 + e^{2B}(dr^2 + dz^2) + \rho(r)^2 e^{2C}d\Omega^2_{D-3}. \tag{23}$$

As usual in the Euclidean signature, the imaginary time must be identified with period equal to the inverse temperature, $t_E \in [0, 4\pi/(D-4)e^{A-B}]$.

1. The cone

The Euclidean double-cone metric over the base $S^2 \times S^{D-3}$ reads

$$ds^2_{\rm cone} = dR^2 + R^2\left(\frac{1}{D-2}(d\chi^2 + \sin^2\chi\kappa^2 d\tau^2) + \frac{D-4}{D-2}d\Omega^2_{D-3}\right), \tag{24}$$

where χ is the angle of $S^2_{\tau,\chi}$ ranging within $(0, \pi)$; $\tau = t_E$ and therefore $\kappa = \frac{1}{2}(D-4)e^{A-B}$ is the surface gravity of the black string.

Comparing (23) with (24) one gets

$$R(r,z) = e^{C(r,z)}\rho(r)\sqrt{\frac{D-4}{D-2}}, \qquad \sin\chi(r,z) = \frac{\sqrt{(D-4)f(\rho(r))}}{\kappa\rho(r)}e^{A(r,z)-C(r,z)}. \tag{25}$$

Next, one rewrites the remaining components of the cone metric in the (r, z) coordinates,

$$dR(r,z)^2 + \frac{1}{D-2}R(r,z)^2 d\chi(r,z)^2 = c1\,dr^2 + c2\,dz^2 + 2c3\,dr dz, \tag{26}$$

where

$$c1 = (\partial_r R)^2 + \frac{1}{D-2}R^2(\partial_r\chi)^2, \qquad c2 = (\partial_z R)^2 + \frac{1}{D-2}R^2(\partial_z\chi)^2, \qquad c3 = (\partial_r R)(\partial_z R) + \frac{1}{D-2}R^2(\partial_r\chi)(\partial_z\chi). \tag{27}$$

Comparing with (23) one concludes that the cone geometry will indeed approximate the regions of the black string's spacetime where $c1 = c2 = e^{2(B,r,z)}$ and $c3 = 0$.

As an additional test, one can compare the Kretschmann scalar curvatures of the numerical and the cone metrics. For the cone this scalar is given by

$$K \equiv R_{abcd}R^{abcd} \propto \frac{1}{R^4}, \tag{28}$$

where the proportionality constant depends on the dimension (in 5D it is 48, in 6D it is 72, in 7D it is 320/3 etc). For the metric (23) the expression for K is cumbersome but it is straightforward to obtain.

2. The scaling and the wiggles

In order to test the scaling (2) one examines the behavior of a characteristic length scale of the nearly pinching strings as a function of some parameter along the NUBS branch. The characteristic variable whose behavior we test is $R_{\rm min}$. Identifying a good parametrization[8] appears to be a difficult task in our case, since many "potential parameters," such as $\hat{\kappa}$ or $\hat{S}$, for instance, are too noisy at the near merger limit due to numerical errors. In this paper, we use two different parameterizations: (i) By $p_1 \equiv \hat{L}_{\rm hor}$, which monotonically grows and seems to tend to a finite value,

[8] A good parameter should be defined on both sides of the merger, i.e. along BHs and NUBSs branches, and it should be analytic at the merger point. In this case, the scaling exponent would not be affected by a transformation to another parametrization, provided the transformation is analytic. In the critical collapse context this is related with the notion of "universality," i.e. independence of parametrization.

$\hat{L}^{\max}_{\rm hor}$, at large nonuniformity; (ii) By $p_2 \equiv B_0^{-1}$, which is our low-level parameter, that apparently tends to zero at the merger. While the first parametrization is continuous across the merger point,[9] it is not obvious that it is also analytic at this point. As for the second parametrization—it becomes not analytic at the merger. The scaling (2) will be confirmed if the graph of $\log(R_{\rm min})$ against $\log(\delta p_i)$ for $i = 1$ and $i = 2$ will be on average linear with periodic wiggles about it. The slope of the linear fit to the curve will provide γ_i and the period of the wiggles about the fit is directly measured.

III. NUMERICAL IMPLEMENTATION

We fix the asymptotic length of the compact circle to the critical value $L = L_c = 2\pi/k_c$, where k_c is the critical Gregory-Laflamme wavenumber (see Table 1 in [30]), and generate the NUBS solutions by varying the constant $B_0 \equiv B|_{z=L/2}$ in (12).

The actual solution of the elliptic Eqs. (6) is obtained using *relaxation*. To this end the equations are discretized on a lattice covering the domain of integration $\{(r, z)\colon 0 \le z \le L/2, 0 \le r \le r_a\}$, where r_a is the location of the outer boundary. The equations are written using a finite difference approximation (FDA) which is second order in the grid spacings. The relaxation of the nonlinear Eqs. (6) is achieved by incorporating a Newton iteration. Specifically, the fields at an interior grid point (i, j) are updated according to

$$\Psi^{\rm new}(i, j) = \Psi^{\rm old}(i, j) - \omega\left[\frac{\mathcal{E}_\Psi(i, j)}{\partial\mathcal{E}_\Psi/\partial\Psi(i, j)}\right]^{\rm old}, \qquad (29)$$

for $\Psi = A$, B and C; $\mathcal{E}_\Psi(i, j)$ is the FDA equation of motion for Ψ and ω is a numerical factor. In the basic Gauss-Seidel relaxation method ω is set to unity. In our case we find that choosing $\omega = 1$ for all fields causes divergence of the code. However, taking $\omega_B < 1$, that is under-relaxing B, stabilized the scheme (usually we used $\omega_B \simeq 0.5$).

At the boundaries of the domain, boundary conditions (b.c.) are incorporated. While, for Neumann b.c. the update procedure is similar to (29), for Direchlet or Robin (mixed) b.c. the equations are not solved. We use Direchlet condition (12) to update B at the horizon. The Robin boundary conditions are used at the outer boundary, where A and B are updated according to (13): $A(z, r_a) = A(z, r_a - \Delta r) \times [r_a/(r_a - \Delta r)]^{D-4}$ and $B(z, r_a) = B(z, r_a - \Delta r)[r_a/(r_a - \Delta r)]^{D-4}$, where Δr is the grid-spacing. C is updated according to

$$C^{\rm new}(r_a) = (1 - \mu_C)C^{\rm old}(r_a) + \mu_C\left[C(z, r_a - \Delta r)\frac{r_a}{r_a - \Delta r}\right]^{\rm old}. \qquad (30)$$

where $0 \le \mu_C < 1$ is the "inertia" parameter. We generate most of our solutions using large inertia i.e. $\mu_C \le 0.05$. Using no inertia caused divergence. All other b.c. are Neumann.

The relaxation begins with specifying an initial guess for the fields. Then, we sweep the grid using the red-black ordering and update the fields according to (29). The sweeps are repeated until the residuals drop below certain predefined tolerance (typically, 10^{-7}).

A. The hierarchy of meshes

One of the disadvantages of relaxation methods is their relatively slow convergence. A well-known technique intended to accelerate the convergence is the full adaptive storage multigrid method, see e.g. [31]. Unfortunately, in our case we could not find convergent multigrid implementation.[10]

The method that we found to work well makes use of several grids but in a different from the full multigrid fashion. We begin with some initial guess on the coarsest grid and completely relax the equations using the algorithm described in the previous subsection. The solution is then interpolated into a finer grid where it is regarded as an initial guess. The equations are relaxed on this grid too, and the solution is passed to the next finer grid. The procedure is repeated on a desired amount of grids. The oneway manner that we propagate the solution along the grid hierarchy is to be contrasted with the bi-directional (V-cycle) communication between grids that is utilized by full multigrid methods.

We construct the mesh hierarchy using 2:1 refinement. Furthermore, in this sequence the radial extension of a finer mesh is taken to be half the extension of the previous mesh. The truncation is basically done because the high resolution delivered by dense grids is only necessary near the horizon where the fields are most variable.[11] Note that number of the grid points in radial direction is conserved in this hierarchy. The boundary conditions used on finer grids do not change, except at the outer boundary, where we keep the fields at the values obtained on the coarsest grid. We verify that no mismatch between our NUBS solutions on any two subsequent grids arises along this boundary. Figure 2 illustrates the hierarchy and the field B on it in 6D.

[9]On the BHs side we can define "$\hat{L}_{\rm hor}$" as a (normalized) proper length of the compact circle along the symmetry axis $r = 0$ and between the poles of black hole along the horizon.

[10]It does not blow up, but the residuals just stop decreasing below certain limit. See Appendix B for further discussion of the phenomenon.

[11]Hence our refinement is in tune with the adaptive mesh refinement (AMR) approach.

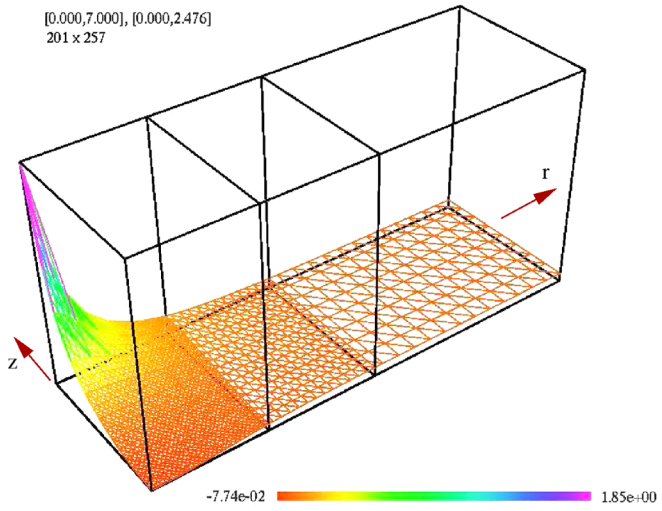

FIG. 2 (color online). The grid hierarchy, 3 meshes are shown. While the coarsest mesh covers the entire domain, the finer grids extend only to half size of the previous coarser mesh. The displayed field B (as well as A and C) is most variable near the horizon, justifying this "AMR"-type construction.

The initial guess on the coarsest mesh requires some caution. A priori we do not have a natural choice, so we use the simplest $A = B = C = 0$ substitution. We found that this guess is relaxed effectively only for B_0 below certain value (which roughly corresponds to mildly deformed strings) for larger B_0's it leads to a very slow convergence or to divergence. However, using a solution obtained at smaller B_0 as an initial guess for higher B_0's prevented the code from crushing and improved the convergence rate.

Despite using this trick, on each particular initial grid we were able to find solutions only up to certain maximal B_0. For larger B_0's the method diverges no matter how we tune up the parameters. In this case, we could continue to larger B_0's by increasing the density of the initial mesh. A significant gain in the convergence rate was achieved by feeding the available lower resolution solution as an initial guess.

As a result, after finding the NUBS branch we end up with a family of several initial meshes having different resolutions, and the multigrid hierarchy attached to each one of them. We verify that the physical measurables obtained on various meshes within the hierarchy converge quadratically. When we had a family of several initial grids with overlapping parameters we verified the convergence rate as a function of the resolution on the initial mesh. Figs. 3–5 are made in six dimensions where we have such an overlap. The convergence rate of the quantities shown in figures is nearly second order.

A verification of the constraints as well as further technical details of the numerical procedure are found in Appendix B.

Overall, we find that the method performs very efficiently in lower dimensions and small nonuniformities.

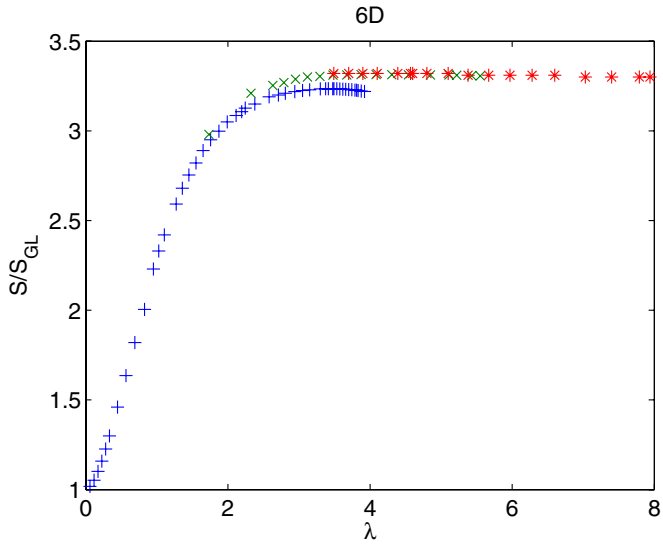

FIG. 3 (color online). The normalized entropy (18) of NUBSs in 6D as a function of λ. Shown are the solutions obtained using three mesh resolutions: low (pluses), medium (crosses) and high (stars), obtained by halving the grid-spacings. In the region where all three overlap we observe nearly second order convergence. The NUBSs are more entropic than that of the critical uniform string. In the limit of large λ the entropy reaches saturation. The bending that shows up beyond certain λ at lower resolution, at a higher resolution moves to larger λ's in the manner that does not form clearly convergent sequence.

For large nonuniformities the convergence slows down and, in general, violation of the constraints grows. We could overcome the problems and accurately get the solutions with stronger horizon deformations by increasing the resolution of the numerical lattice. We had to stop when the mesh size made the relaxation time unreasonably long. In higher dimensions the problems are more pronounced and begin earlier. In addition, the range of the parameters ω_B

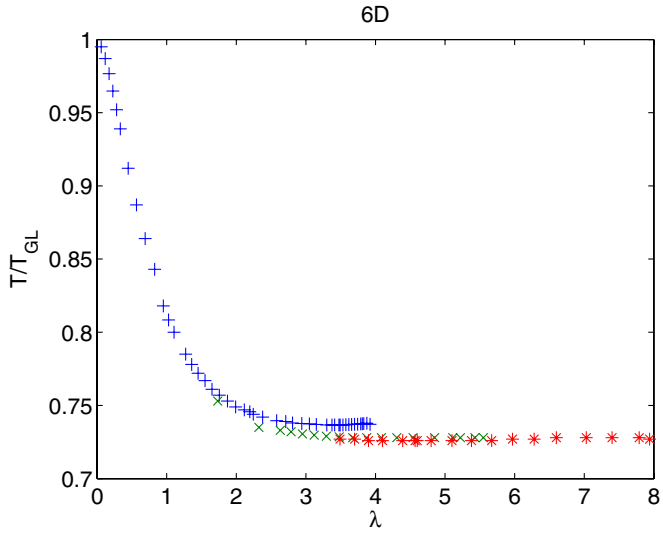

FIG. 4 (color online). The temperature in 6D as a function of λ. Same conventions as in Fig. 3.

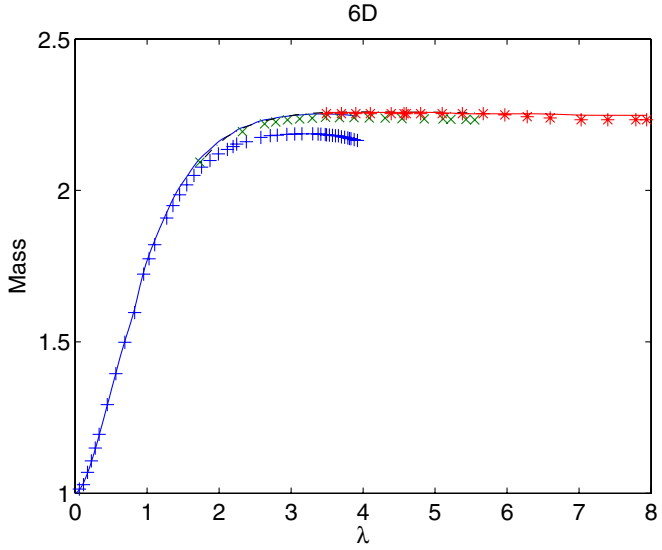

FIG. 5 (color online). The mass as a function of λ in 6D, same conventions as in Fig. 3. The markers designate the mass computed from (15), the solid lines indicate the result obtained by integration of the first law, see (B3). Both methods agree well and the agreement improves at higher resolution.

and μ_c, for which the relaxation converges, shrinks. In practice, using our current method we were only able to get the NUBS solutions in the dimensions between six to eleven. The following section summarizes our findings.

IV. RESULTS

We construct the branch of nonuniform black strings in dimensions $6 \leq D \leq 11$ and extend it deep into nonlinear regime. In 6D we find good agreement with previous results [18,19] in the range of λ's obtained in these works, $\lambda \simeq 4$ in [18], and $\lambda \simeq 6$ in [19], and continue the branch up to $\lambda \simeq 8$. Below we describe the behavior of the characteristic physical variables and their dependence on the dimension.

The typical behavior of the (normalized) entropy (18) in the verified range of the dimensions is depicted in Fig. 3. The key feature here is that the relative entropy grows with λ, so that NUBSs are more entropic than the uniform critical string. In $D \leq 9$ we find that at large λ's the entropy asymptote to certain limiting value. These limiting values are listed in Table I and they estimate the entropy of the merger string. In higher dimensions our numerical method does not allow extending the branch that far, in this case the numbers in the table are only lower bounds on the asymptotic $\hat{S}$'s. We find that the $\hat{S}(\lambda)$ curve steepens as D grows and the saturations occurs earlier. For example, while in 6D this happens around $\lambda \simeq 3$, in 9D $\hat{S}$ reaches saturation just above $\lambda \simeq 1.5$. The entropy of the nearly pinching strings decreases with the dimension.

We note that the $\hat{S}$ curve has the back-bending reported in [19]. However, the variation of $\hat{S}$ in the bending, $\delta S/S$, is less than a percent in our range of λ's. In addition, from the figure we learn that the specific value of λ_{bb} beyond which the curve bends depends on the resolution of the numerical lattice used to find the solution, in a way that an increase in resolution increases λ_{bb}. In 6D (shown in the figure) we use a sequence of three resolutions with grid spacings h, $h/2$ and $h/4$. The resulting λ_{bb}'s are approximately 3.5, 4.5, and 5.5, which does not seem to form a convergent sequence. Similar behavior is gotten in higher D's as well.

The typical dependence of the temperature (17) on λ is depicted in Fig. 4 which shows that the NUBSs are cooler than the critical GL string. The temperature decreases with λ and in $6 \leq D \leq 9$ it is seen to tend to certain limiting values. In higher dimensions our numerics loses stability before the saturation is achieved. The minimal attained temperatures are listed in Table I. The features such as the steepening of the $\hat{T}(\lambda)$ curve in higher dimensions and the bending are similar to those observed for the entropy. The temperature of the nearly pinching strings in various dimensions increases with D.

In Fig. 5 we plot the normalized mass as a function of λ. The mass is computed in two ways: (i) From the asymptotic charges according to (15), the result is designated by markers; (ii) Integrating the first law (20) according to (B3), this is represented by solid line. The figure demon-

TABLE I. The thermodynamic and the geometric variables at the maximal λ to which we could extend the NUBS branch. In the dimensions between six to nine the behavior of the variables is similar to this plotted in Figs. 3–5 and 7. Namely, in these dimensions the listed numbers are close to the asymptotics. ($R_{\min}$ does not reach saturation but continuously decreases. The shown values correspond to the minimal attained $R_{\min}$.) In higher dimensions the shown numbers are not asymptotics, but only bounds on the true limiting values.

D	$\lambda_{\max}$	$\hat{m}$	$\hat{T}$	$\hat{S}$	$R_{\max}$	$R_{\min}$	$\hat{L}_{\rm hor}$
6	8	2.26	0.73	3.3	1.75	0.103	1.45
7	4.45	2.37	0.793	3.25	1.57	0.16	1.43
8	4.1	2.28	0.86	2.83	1.42	0.156	1.34
9	1.7	1.98	0.91	2.3	1.32	0.3	1.23
10	0.46	1.5	0.96	1.7	1.22	0.64	1.07
11	0.2	1.14	0.99	1.22	1.13	0.81	1.04

TABLE II. The scaling exponents γ in $R_{\min} \propto \delta p^{\gamma}$ in various dimensions for two parameterizations. The first row shows the upper bounds on γ in the parametrization by $\hat{L}_{\rm hor}$. The second row is the lower bound on γ in the parametrization by B_0^{-1}. Distinct γ's for a given D reflect the fact that the transformation between the parameterizations is not analytic.

D	6	7	8	9
γ in $\hat{L}_{\rm hor}$	0.6	0.54	0.41	0.33
γ in B_0^{-1}	2.1	1.8	2.2	1.4

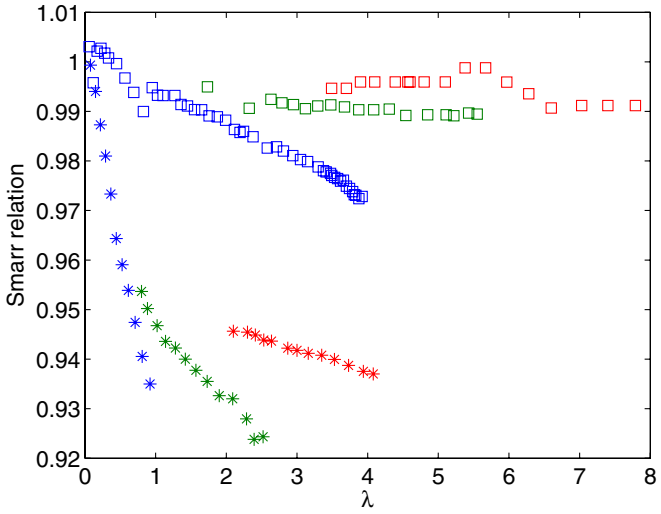

FIG. 6 (color online). The Smarr formula (19). Shown are the ratios between the two sides of (19) in 6D (squares) and 8D (stars). In each dimension, there are three sequences of points obtained at three numerical resolutions, with the sequence at largest λ corresponding to the largest resolution. In either case, the points concentrate near 1 such that the violation of Smarr's relation never exceeds the 10% level.

strates that both methods yield comparable results and the agreement further improves as we increase the resolution. In all verified dimensions the mass along NUBS branch is higher than that of the critical string. All other features of the mass curve are similar to those of the entropy curve. At large λ, in $6 \leq D \leq 9$, the mass reaches saturation, the asymptotic values recorded in Table I. In higher dimensions the table shows only the maximal masses obtained rather than asymptotics. The mass of the nearly pinched strings is a decreasing function of the dimension.

Smarr's formula (19) relates the local horizon variables S and T with the asymptotic ones, m and τ, and as such it is an important indicator of *global* accuracy of a numerical method.[12] In Fig. 6 we plot the ratio between the two sides of (19) in six and eight dimensions. We observe that in general the formula is well satisfied. The scattering of the points does not exceed 10%, a large fraction of which is probably due to inaccurate τ. For a given resolution the accuracy decreases for progressively nonuniform solutions. However, the accuracy improves at higher resolutions, indicating convergence.

To analyze the geometry of the NUBSs we plot in Fig. 7 the minimal and the maximal areal radii of the horizon and its proper length along the compact circle as a function of λ. We find that while $R_{\min}$ shrinks monotonically with λ,

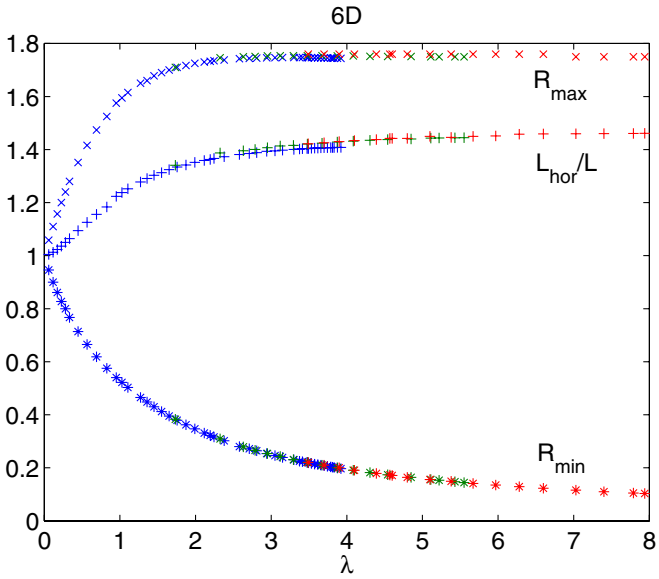

FIG. 7 (color online). The typical behavior of the geometric variables: $R_{\min}$ decreases steadily with λ, $R_{\max}$, and $\hat{L}_{\rm hor}$ asymptote to finite values. Same conventions as in Fig. 3.

$R_{\max}$ and $\hat{L}_{\rm hor}$ asymptote to finite values in the large λ limit. The behavior of the curve $R_{\max}(\lambda)$ is again similar to the behavior of the entropy. The $\hat{L}_{\rm hor}(\lambda)$ curve is similar too, with the only difference that it does not have any backbending. As the dimension grows the asymptotic values of $R_{\max}$ and $\hat{L}_{\rm hor}$ are getting smaller, see Table I.

Figure 8 shows the embedding (21) of the black-string horizon into flat space. The maximal and the minimal radii of the horizon are explicitly seen to occur at $z = 0, L$ and at $z = L/2$ respectively. The proper length of the circle along $r = \text{const}$ is maximal at the horizon but for large r, $\hat{L} \to 1$

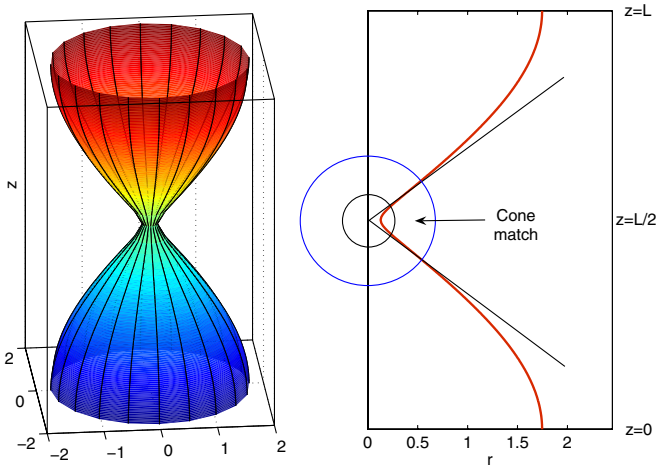

FIG. 8 (color online). The embedding of the string's horizon into flat space (21). The right panel shows the cone and the region (between the circles) where the local geometry is compared with the cone.

[12]It turns out that the tension τ along the NUBS branch cannot be extracted accurately enough in our numerical implementation. However, this fact does not have major impact on the accuracy of the Smarr relation. See Appendix B for analysis and discussion.

exponentially fast. Note that the transition from a uniform to a nonuniform black string causes an expansion of the compact circle near the horizon. In this sense we have an Archimedes effect for nonuniform black strings. The effect weakens in higher dimensions, see Table I.

A. The local cone

We compare the local geometry in vicinity of the waist of strongly nonuniform strings with the cone metric. The relevant spacetime region is illustrated in Fig. 8. The cone sketched in the right panel is predicted to approximate the local merger geometry of the marginally pinching string. In this case one would expect that a nonpinching, but strongly deformed string still carries signs of the cone geometry in the region bounded by the circles shown in figure. We will now demonstrate that with high precision the geometry near the waist is indeed conelike.

We explicitly compare the numeric and the cone metrics in six dimensions where we have our most nonuniform solutions and the highest resolutions. First, according to (25) we obtain R and χ in terms of (r, z). The extraction of χ appears to be delicate [25] because χ is obtained from $\sin\chi$, which for our numerical solutions with finite λ behaves somewhat differently from what it should for the cone. Specifically, at the axis $z = L/2$, that corresponds to $\chi = \pi/2$, the cone must have $\sin\chi = 1$. However, since the cone apex is missing at finite λ, $\sin\chi$ obtained from (25) happens to be greater than 1 at small r's, see Figs. 8 and 9. At the same time, Fig. 9 shows that along the axis sine is close to 1. The peak in the curve, that appears because the cone's tip is missing, drifts to the origin as λ grows indicating that the cone apex becomes resolved better in the large λ limit.

Clearly, having $\sin\chi|_{\text{axis}} > 1$ obstructs the extraction of χ. A practical remedy to the problem was suggested in [25], where the sine was "renormalized" by its value at the axis, forcing it to the correct, $\sin\chi_{\text{axis}} = 1$, value. The renormalization is achieved by

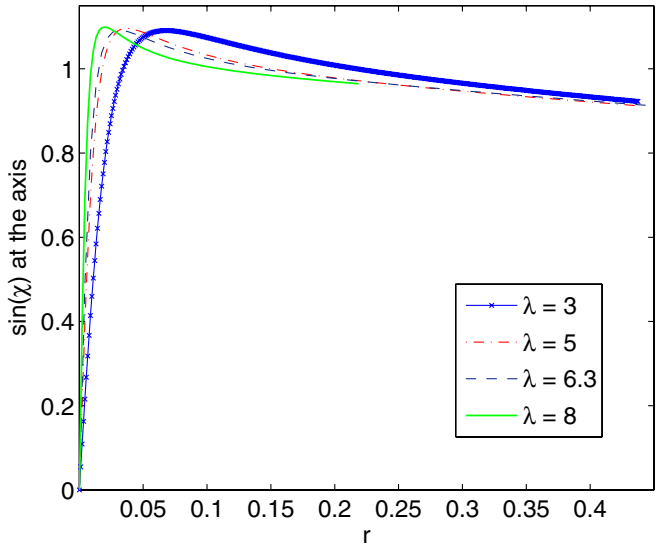

FIG. 9 (color online). $\sin\chi$ along the $z = L/2$ axis as determined from (25) in 6D. For the cone $\sin\chi|_{\text{axis}} = 1$, but for a finite λ NUBS this is not so. Since the cone tip is missing, the curve initially climbs steeply to values greater than 1, stays close to unity and finally deviates from one farther away from the waist. For increasingly nonuniform strings the peak tends to the origin and the entire curve gets consistently closer to unity. This indicates that the cone tip is closer approached. The markers in one of the graphs designate the actual resolution of the numerical lattice.

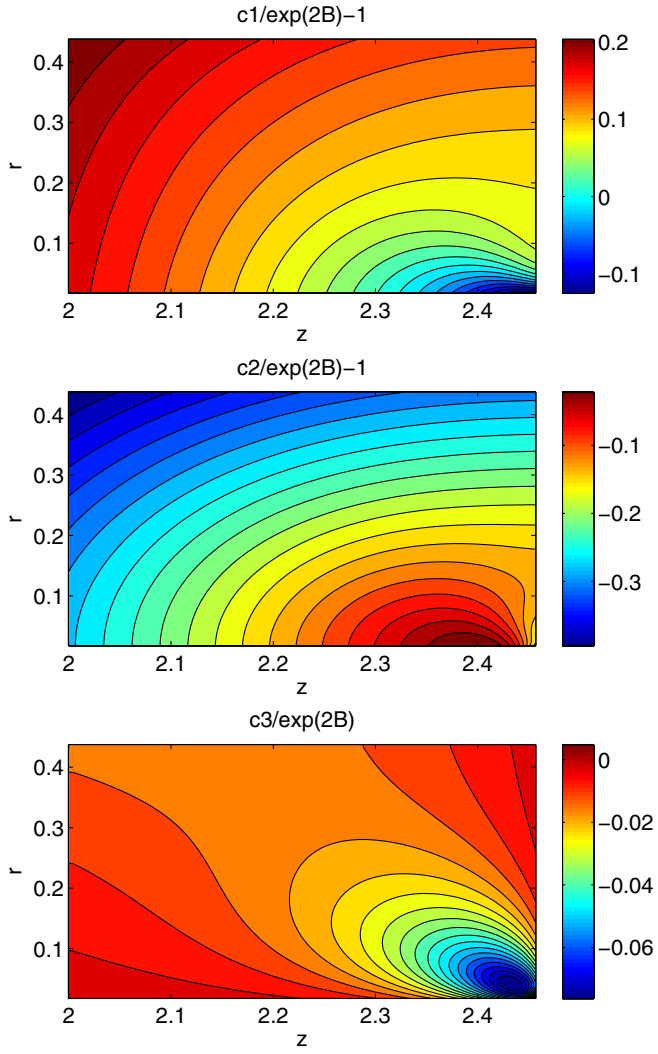

FIG. 10 (color online). 6D; $\lambda \simeq 6.3$. The metric components (27) that must satisfy $c1 = c2 = e^{2B}$ and $c3 = 0$ if the cone indeed approximates local geometry near the waist which is located at the bottom right corner. $c1$ and $c2$ agree very well with the cone prediction: we see approximately 90% match slightly away from the corner. $c3$ is 2 orders of magnitude smaller than $c2$ and $c1$, that is consistent with the cone prediction as well. The subdomain shown here is covered with the numerical lattice of approximately 200×200 mesh points.

$$\sin\chi(r,z)|_{\text{corrected}} = \frac{\sin\chi(r,z)}{\sin\chi_{\text{axis}}}, \tag{31}$$

where in order to normalize outside of the axis one finds $\sin\chi$ at the axis and proceeds along $R = \text{const}$ curves using this value.

Having obtained R and χ, we determine the metric components (27) $c1$, $c2$ and $c3$ and plot them in Figs. 10 and 11 for $\lambda \simeq 6.3$ and $\lambda \simeq 8$ respectively. There is an excellent agreement with the cone prediction. It is required that $c1 = c2 = e^{2B}$ and from the figures we learn that while $c2$ and $c1$ differ from e^{2B} by several tens of percents far away from the waist, the match grows to a level of more then 90% closer to the corner. Expectedly, the agreement worsens again in the immediate vicinity of the apex, see Fig. 8. As for $c3$, which must vanish for the cone—it is 2 orders of magnitude smaller than $c2$, $c1$ in the relevant region, and this is indeed consistent with the prediction.

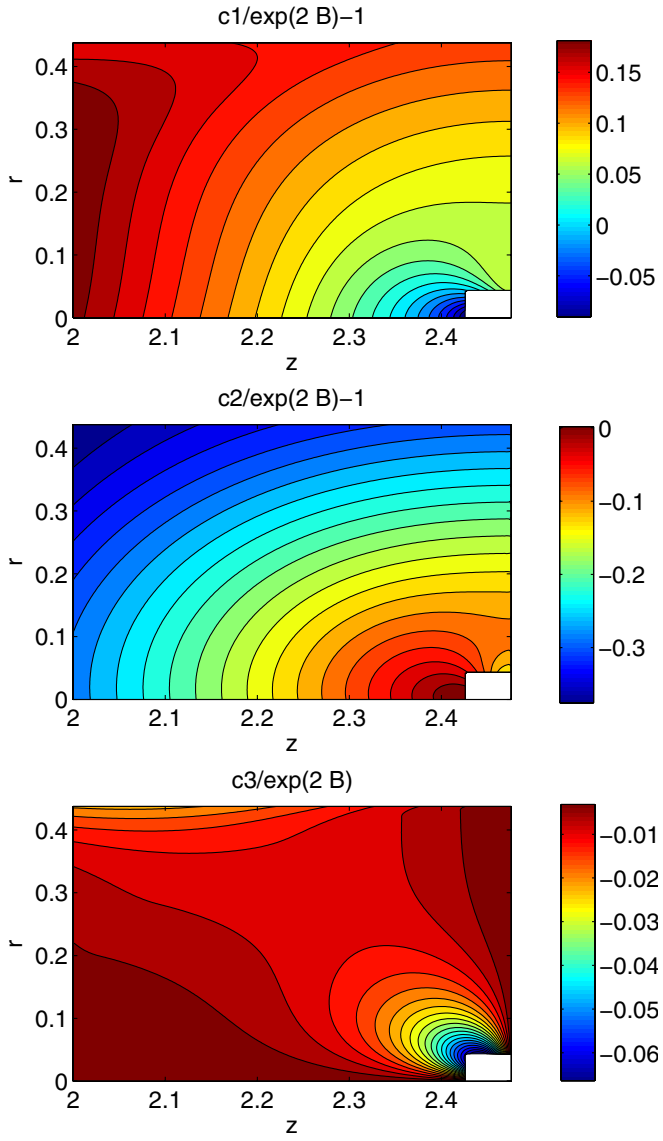

FIG. 11 (color online). 6D. $\lambda \simeq 8$ and we use same conventions as in Fig. 10 but remove the apex. The agreement with the cone prediction is somewhat better than in Fig. 10.

Another test involves comparison of the Kretschmann curvature invariants computed for the numerical and the cone metrics, see Fig. 12. The plot indicates that the invariants are comparable around the waist, where the mismatch between them is only about 10%.

Next we verify the scaling (2). A characteristic quantity with dimensions of length whose scaling we will test is the minimal areal radius of the horizon R_{min}. It is measured directly from the metric and hence it is the cleanest, from the numerical point of view, variable. One of the parameterizations of the NUBS branch that we use in this paper is given by $p \equiv \hat{L}_{\text{hor}}$. The horizon length apparently remains finite at the pinch-off, and as we saw it does not exhibit any bending. Assuming that $\hat{L}_{\text{hor}}$ is growing monotonically we obtain the limiting length, $p* = \hat{L}^{\text{max}}_{\text{hor}}$ by extrapolation.

Figure 13 plots $\log(R_{\text{min}})$ as a function of $\delta p \equiv \log(\hat{L}^{\text{max}}_{\text{hor}} - \hat{L}_{\text{hor}})$ in six, seven, eight and nine dimensions. Figure shows that for small p's the scaling of R_{min} is not a power-law. However, the behavior is approaching a power-law dependence in the $p \to p*$ limit. This is most pronounced in 6D where we have the longest data series. The "runaways" of the data points that appear at the end of each sequence with a given resolution is probably related to the loss of accuracy.

The insets show several points that correspond to the largest nonuniformity. These points can be fit quite accurately by a straight line (shown), and this indicates the power-law scaling. The corresponding exponents are given by the slope of the fits and they are summarized in Table II. These are only approximate values because of the numeri-

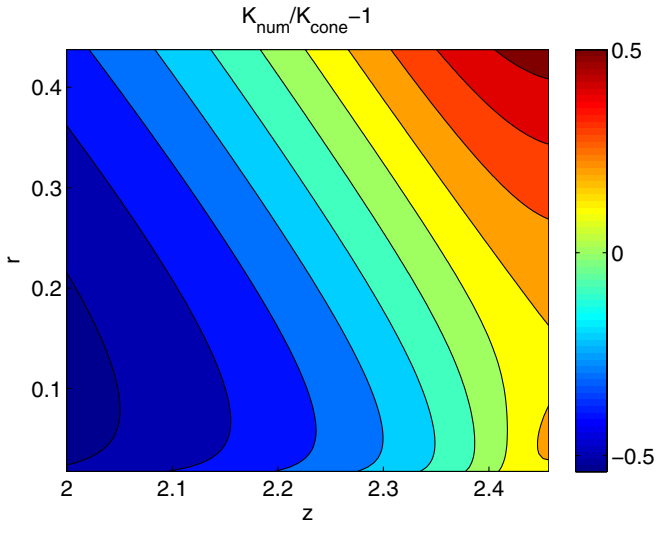

FIG. 12 (color online). 6D. A comparison of the Kretschmann invariants computed for the cone and the numerical black-string with $\lambda \simeq 6.3$. A good match is in the vicinity of the "waist," which is located at the right bottom corner of the figure.

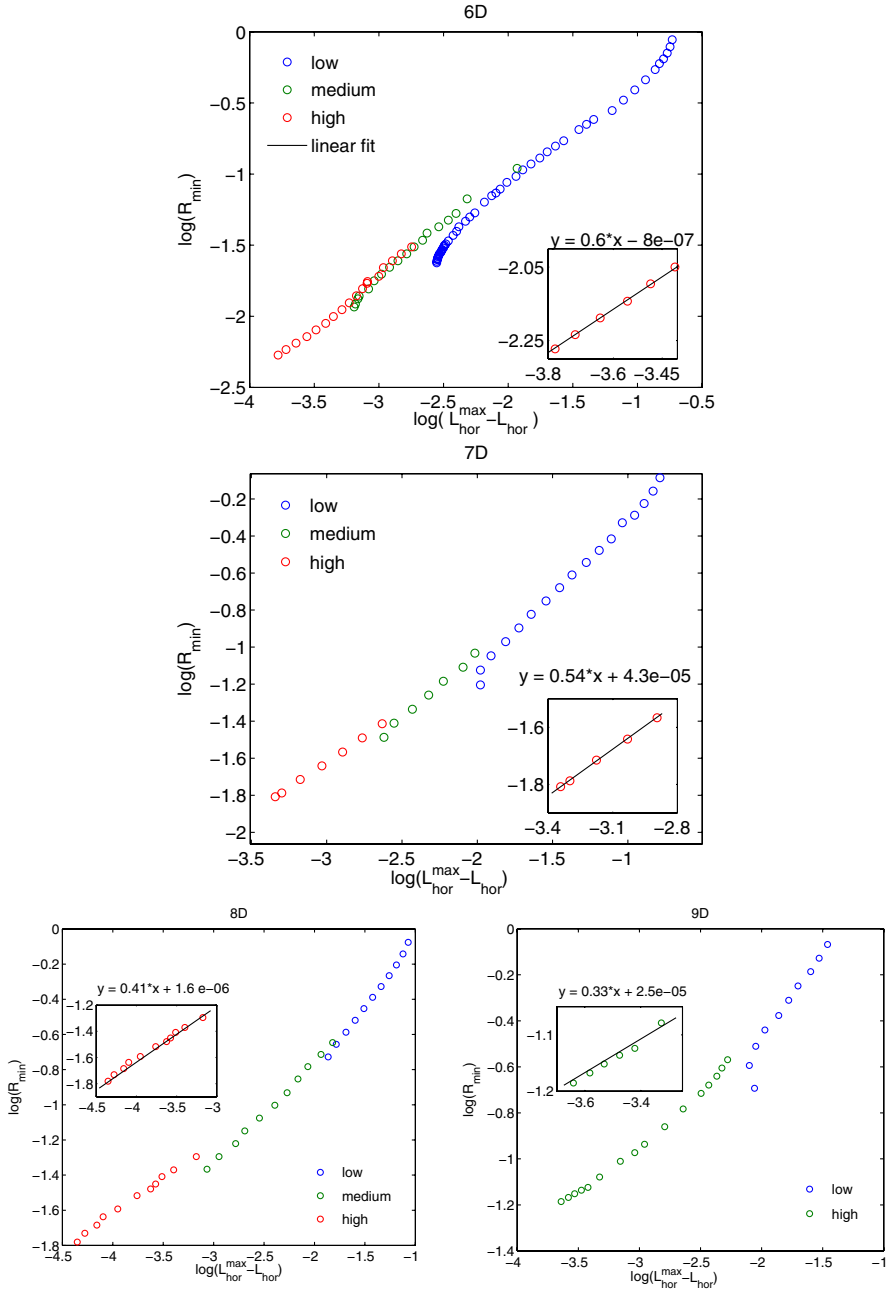

FIG. 13 (color online). The scaling of $\log(R_{\min})$ as a function of $\delta p = \log(\hat{L}^{\max}_{\rm hor} - \hat{L}_{\rm hor})$ in various dimensions. We show the sequences of data points obtained at several resolutions, with the largest resolution sequence corresponding to the smallest δp. The solid line, which is the linear fit, is seen to approximate the data points well. This indicates that at large λ's we have a power-low. The corresponding exponents are given by the prefactors in the displayed fitting equations.

cal errors related to the fitting procedure (whose accuracy is within 5%), and other manipulation such as extrapolation that we used to find $p*$ etc. Besides, the values in table should strictly speaking be regarded as upper bounds on the exponents, rather than the exponents themselves. It is hard to say how close to the actual γ's the bounds are, but at least in six and seven dimensions they seem to provide a good estimate, see Fig. 13.

In principle, we could parameterize the NUBSs branch differently, for instance, by κ or by $\hat{S}$. In practice however, all measurables except $\hat{L}_{\rm hor}$ have the back-bending that hampers determination of their asymptotic values, which are crucial for forming δp. On the other hand, the control parameter, B_0^{-1}, that we use to generate our solutions is a monotonic function of λ, and it naturally parameterizes the NUBSs branch. A disadvantage of this parametrization is that it is not defined on the BHs side. Figure 14 depicts $\log(R_{\min})$ vs $\log B_0^{-1}$. The behavior is not a power-low for mildly deformed strings, however as indicated by the straight lines shown in figure, the dependence becomes

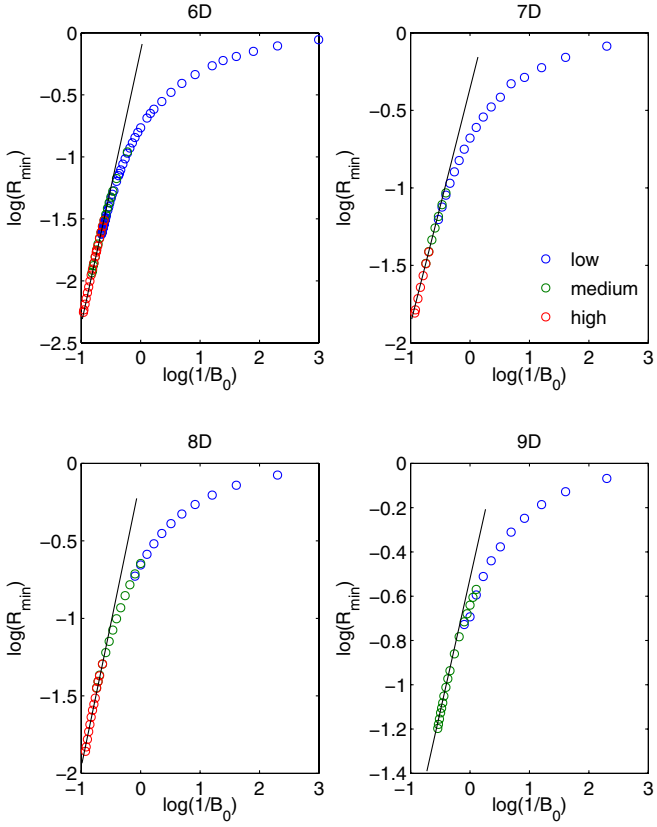

FIG. 14 (color online). The scaling of $\log(R_{\rm min})$ as a function of $\delta p = \log(B_0^{-1})$ in various dimensions. Same conventions as in Fig. 13. In the limit of large deformations the scaling is clearly a power-law as indicated by the shown linear fit.

such in the near-merger regime. The slopes of the lines provide lower bounds on the critical exponents γ, we list these in Table II and observe that $\gamma \sim 2$ in all recorded dimensions. Comparing γ's in both parametrization we see that they are distinct, therefore the parameterizations are not analytically related.

Having estimated the exponents we can ask about the fine structure, or the "wiggles," that according to the prediction should appear as a wavy structure about the linear fit in Figs. 13 and 14. By examining Fig. 13 one infers that in six and seven dimensions there are no any wiggles in the range of the achieved nonuniformity, and in higher dimensions the accuracy of the data is insufficient for deciding about existance/absence of the wiggles. From Fig. 14 it follows that the wiggles do not appear in any of the plots.

V. DISCUSSION

Our numerical construction of the branch of the NUBS solutions confirms the trends observed in the perturbative analysis of [6] and lends further support to the phase diagram 1. We managed to extend the solutions branch into strongly nonuniform regime and this allowed us to estimate the physical parameters of the nearly pinching strings, see Table I. We expect the estimates to be good in $6 \leq D \leq 9$, where we could approach the merger closely, and they are only bounds (upper or lower, depending on the variable) in higher dimensions.

It follows that when the spacetime dimension grows the mass and the entropy of the near-merger solution decrease and their temperature increases. This is in accordance with the expectation [6] that in higher dimensions the trends in the behavior of the (normalized) thermodynamic variables are reversed, see diagram 1. This is best illustrated by the temperature, which is expected to change its trend in $D \gtrsim 12$. One notes that while in 6D the limiting temperature along the branch is smaller than 1 by about 30%, in 11D it is smaller than 1 by less than 1.5%. (Of coarse, in this dimension we have not extended the branch into really asymptotic regime. However, the shape of the curve $\hat{T}(\lambda)$ suggests that the asymptotic value is not much smaller than the estimate.)

It is interesting to note that our numerical method performs well for weakly deformed strings in $D \leq 11$, but in 12D (and higher) it fails to converge for any, no matter how small, deformations. Recalling that the trends in the temperature are expected to change at about $D \simeq 12$ we tend to attribute this behavior to the fact that due to limited accuracy our numerics is incapable of deciding on the sign of $\hat{T} - 1$, even if it can determine correctly other thermodynamic variables. This probably leads to a conflict that eventually results in the divergence.

Examining our most deformed strings we provide strong quantitative evidence that the local geometry in vicinity of their waist is conelike. The deviation from the cone geometry is less than 10%, which leaves little room for any solution other than the cone. The cone's presence is further (indirectly) supported by appearance of the power-law scaling (2).

The power-law behavior (more precisely—its onset) of the characteristic length scale $R_{\rm min}$ is observed and depicted in Figs. 13 and 14. The estimates of the corresponding critical exponents are collected in Table II. We used two parameterizations that are not analytically related, and hence the corresponding γ's are not equal. While the parametrization by B_0^{-1} is not defined beyond the merger point (along the BHs branch), the parametrization by $\hat{L}_{\rm hor}$ can be made continuous across this point (though it is not obvious if it is analytic at the pinch-off); in this sense $\hat{L}_{\rm hor}$ parametrization is superior.

Proving that $\hat{L}_{\rm hor}$ is analytic at the pinch-off, will qualify the parametrization as "good" (see footnote 8). In this case[13] we can compare the estimated γ's with the prediction of [20], where it is proposed that $\gamma_{\rm th} = 1/4$ in any $D \leq 10$. Clearly, our estimates differ from $1/4$ and there

[13]If $\hat{L}_{\rm hor}$ will not happen to be analytic at the merger, the exponents are incomparable.

can be several reasons for this. First, in general, one should not really expect for the actual exponents to coincide with those obtained in the linear analysis of [20]. Second, our estimates may be too crude and the more accurate γ's will indeed be $1/4$. While this is possible, we believe that at least in six and in seven dimensions our estimates cannot be significantly different from the actual exponents, see Fig. 13. Finally, it is likely that the truth lies somewhere in the middle, and so are the actual values of the critical exponents.

In conclusion, we note that there are still many aspects of the phase diagram 1 awaiting for a confirmation. This includes a construction of the black-hole branch in higher than six dimensions and of the black-string branch in $D > 11$. Despite the progress in understanding the pinch-off geometry reported in this paper, one still might wish to approach the merger closer and to do so also form the "black-hole side." Our current relaxation method seems inadequate for achieving these goals due to its slow convergence and instability at the strongest nonuniformity. We believe that in order to address the mentioned issues our scheme will require major revisions (e.g. finding a stable multigrid implementation), or one would probably have to come up with a completely different approach.

ACKNOWLEDGMENTS

I would like to thank Barak Kol for useful remarks on the manuscript, and Carsten Gundlach and Eric Hirschmann for specific discussions. This research is supported in part by the CIAR Cosmology and Gravity Program, by NSERC and by the British Columbia Knowledge Development Fund. The numerical computations were performed on the UBC vnfe4 cluster and on the Westgrid Glacier cluster.

APPENDIX A: UNIFORM BLACK STRING IN CONFORMAL COORDINATES

The metric of the uniform black string in Schwarzschild coordinates reads

$$\begin{aligned} ds^2 &= ds^2_{\mathrm{Schw}_d} + dz^2 \\ &= -f(\rho)dt^2 + f(\rho)^{-1}d\rho^2 + dz^2 + \rho^2 d\Omega^2_{d-2}, \\ f(\rho) &= 1 - (\rho_0/\rho)^{d-3}, \end{aligned} \tag{A1}$$

where ρ_0 designates the horizon location.

In order to bring the (r, z) part of the metric into the conformal form we change the coordinates such that

$$\begin{aligned} ds^2 &= -f(\rho(r))dt^2 + dr^2 + dz^2 + \rho(r)^2 d\Omega^2_{d-2}, \\ dr/d\rho &= f^{-1/2}(\rho), \\ r(\rho) &= r_0 + \int_{\rho_0}^{\rho} \frac{d\rho'}{\sqrt{1 - (\rho_0/\rho)^{d-3}}}, \end{aligned} \tag{A2}$$

where r_0 is the integration constant, that designates the location of the horizon in the conformal gauge (without loss of generality we choose $r_0 = 0$.) The integration gives

$$r = \begin{cases} \rho_0\sqrt{\frac{\rho}{\rho_0}(\frac{\rho}{\rho_0} - 1)} + \rho_0 \log(\sqrt{\frac{\rho}{\rho_0}} + \sqrt{\frac{\rho}{\rho_0} - 1}), & \text{for } d = 4; \\ \sqrt{\rho^2 - \rho_0^2}, & \text{for } d = 5; \\ -\rho_0 \frac{\pi^{1/2}\Gamma(\frac{d-4}{d-3})}{\Gamma(\frac{d-5}{2(d-3)})} + \rho_2 F_1(-\frac{1}{d-3}, \frac{1}{2}, \frac{d-4}{d-3}, [\frac{\rho_0}{\rho}]^{d-3}), & \text{for } d > 5, \end{cases} \tag{A3}$$

where ${}_2F_1$ is the hypergeometric function.

Our numerical implementation in the conformal coordinates requires knowing $\rho(r)$. Explicit inversion of (A3) exists only in $d = 5$, in any other dimension the inversion must be achieved numerically.

APPENDIX B: DETAILS AND TESTS OF THE NUMERICS

In this appendix we provide further details of the numerical procedure, verify the constraints and describe how the asymptotic charges are obtained.

Table III summarizes the measures of the domain of integration and the sizes of the coarsest meshes in various dimensions. In order to minimize the mesh size (and, as a result, the relaxation time) without compromising accuracy we choose the location of the asymptotic boundary r_a as close to the origin as possible. To achieve this, we try several r_a's and select the minimal one for which the thermodynamic variables S and T undergo less than 0.5% variation if r_a is increased.

TABLE III. Location of the outer boundary r_a and sizes of the coarsest meshes used in various dimensions. $L/2 = \pi/k_c$, where k_c is the critical GL wavenumber, see Table 1 in [30].

D	$L/2$	r_a	Low	Medium	High
6	2.4758	7	201×65	401×129	801×257
7	1.9884	6	121×41	241×81	481×161
8	1.6982	5	101×35	201×69	401×137
9	1.5032	4.5	91×33	181×65	361×129
10	1.3659	4	91×33	181×65	361×129
11	1.2566	3.75	91×33	181×65	$\cdots$

1. Relaxation parameters

The parameters ω_B and μ_C are selected after several trial runs with similar geometry and resolution but with different parameters. Figure 15 shows the behavior of the L_2-norm of the residuals in several cases. (The L_2-norm of matrix M on mesh $[1\ldots N_r]\times[1\ldots N_z]$ is defined by $\|M\|_{L_2}\equiv\sqrt{\sum_{i,j}|M_{i,j}|/N_rN_z}$.) While for some sets of the parameters, the residuals blow up or converge very slowly, for other sets the residuals decrease faster. We have not attempted to locate the "optimal" parameters that might accelerate the convergence rate.

The necessity to use under-relaxation for B, strong asymptotic inertia for C and to fine-tune the corresponding parameters into a narrow range is bewildering. In addition, the convergence/divergence of the code is strongly affected by the initial guess. As described in section III, for the relaxation to converge one has to choose the initial guess "close enough" to the final solution, otherwise the code diverges.

We tend to attribute this unhappy situation to the fact that $(1-e^{2B-2C})/\rho^2$ terms in (6) have "wrong sign" (see also the discussion in [8]). In order to explain what is wrong with the sign, we linearize around some solution. Doing so for $\Psi=B$ or C we end up with the equation of the form $\nabla^2\Psi+m^2\Psi+\ldots=0$, where m depends on the background solution and the position, and the ellipsis designate terms containing first derivatives. Ignoring for a moment these terms we locally get a Helmholtz-type equation. A boundary-value problem for this type of equation is ill-posed if m is smaller than the mesh box, namely, if the tachyon defined by the equation fits into the box and might get exited. This clearly destroys any hopes to relax such an equation numerically.

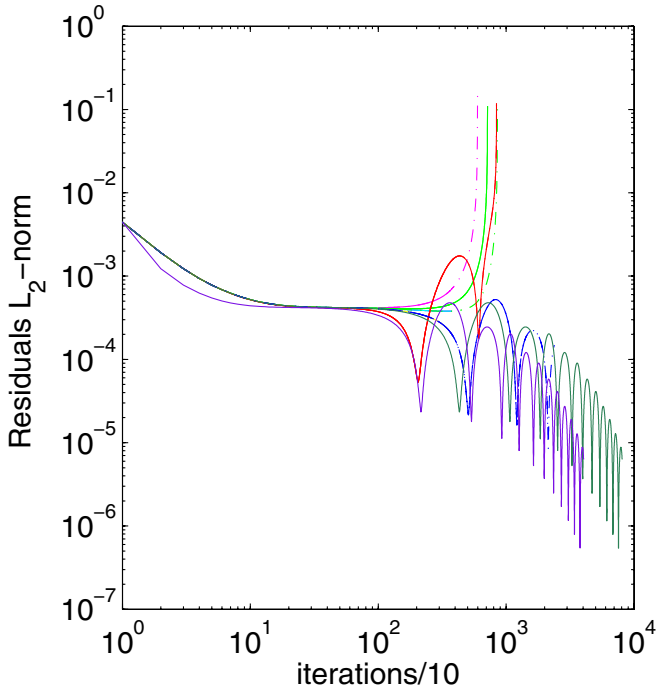

FIG. 15 (color online). A typical behavior of the residuals for several sets of the parameters ω_B and μ_C. In some cases the residuals blow up after finite amount of iterations or show very slow convergence. In other cases the convergence rate is faster.

As for the original set of Eqs. (6), the finite range of the fine-tuned parameters ω_B and μ_C and the sensitivity to the initial guess apparently indicates that while outside of this range the"wrong-sign" causes divergence, inside this range the tachyon is suppressed, and the relaxation converges. We note also that for increasingly nonuniform strings and in higher dimensions the convergence window shrinks (in 10D, for example, $\mu_C<0.01$) The sensitivity to specific values of ω_B, μ_C and to the initial guess may explain the failure of the full multigrid technique. The method operates on grids of variable size and this probably causes the excitation of the tachyon, since it may happen to fit into one of the grid boxes.

Note that at least one of the wrong-sign equations is a direct consequence of working in a higher dimensional spacetime, $D>4$, that has $O(N+1)$ isometry with $D-3\geq N\geq 2$. Indeed, in this case the most general metric is given by

$$ds^2=ds^2_{D-N}(X)+e^{2C(X)}d\Omega^2_N. \tag{B1}$$

Dimensionally reducing the Einstein-Hilbert action over the $\mathbf{S}^N$ sphere and varying it to get the equations (see, for example, Appendix A of [8] where this is elaborated for $N=D-3$), one finds out that C is governed by

$$\triangle C-G(g^{\alpha\beta})e^{-2C}+\cdots=0, \tag{B2}$$

where $g_{\alpha\beta}$ is a metric on X, $\triangle\equiv g_X^{-1/2}\partial_\alpha(g_X^{1/2}g^{\alpha\beta}\partial_\beta)$ and ellipsis designate terms with first order derivatives and second order derivatives of $g_{\alpha\beta}$. The function $G(g^{\alpha\beta})$ depends on the metric $g^{\alpha\beta}$; it is positive if $D\geq 5$ and zero otherwise. The Eq. (B2) has wrong sign in the sense described above, and this property is invariant under gauge transformations of the manifold X.

2. Constraints

A violation of constraints is inevitable in any numerical solution. Here, we examine the convergence rate of the constraints $\mathcal{U}$ and $\mathcal{V}$ as a function of the grid-spacings. In addition, we verify that the (properly normalized) constraints are small.

Usually we solved the equations on the three-grid hierarchy. We computed L_2-norms of both constraints on these grids and checked that typically the ratio $(\|\mathcal{U}\|^h-\|\mathcal{U}\|^{h/2})/(\|\mathcal{U}\|^{h/2}-\|\mathcal{U}\|^{h/4})\gtrsim 3$ and the similar ratio for $\mathcal{V}$ is slightly larger than 1. This indicates that while the constraint $\mathcal{U}$ converges well, the convergence of $\mathcal{V}$ is poor. We tend to attribute this behavior of $\mathcal{V}$ to a growth of the discretization errors near the horizon due to the terms

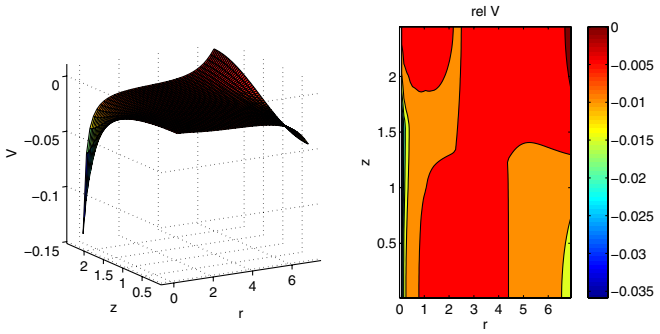

FIG. 16 (color online). $\mathcal{V}$ and rel$\mathcal{V}$ for a strongly nonuniform string ($\lambda \simeq 3.5$) in 6D. The maximal deviation from zero occurs at the horizon, near $z = L/2$. Outside this location the constraint is small. The relative constraint is small too. Altogether we conclude that the constraint is well satisfied.

containing the singular $1/\sqrt{f}$. We will demonstrate now that $\mathcal{V}$ is actually very small everywhere except in the horizon vicinity.

In order to get an idea of how well the constraints are satisfied, we define the "relative constraints": rel$\mathcal{U} \equiv \mathcal{U}/\sum|\text{terms in } \mathcal{U}|$ and rel$\mathcal{V} \equiv \mathcal{V}/\sum|\text{terms in } \mathcal{V}|$, where the sum is over the absolute values of all additive terms forming $\mathcal{U}$ or $\mathcal{V}$. In Fig. 16 we depict $\mathcal{V}$ and its relative value. $\mathcal{V}$ is maximal near the horizon around $z = L/2$ and it is small everywhere else. On the other hand the relative constraint is *small* at this corner, but it is large along the remaining section of the horizon (and its neighborhood), where the $\mathcal{V}$ itself is small (typically of order of 10^{-3}–10^{-2}). Therefore, both plots are complimentary and together they indicate that the constraint is well satisfied. The peak that $\mathcal{V}$ has at the horizon, see figure, gets sharper at higher resolution, but at the same time it also moves towards the corner. This is why the L_2-norm of $\mathcal{V}$ showed poor convergence.

The second constraint $\mathcal{U}$ and its normalized counterpart are illustrated in Fig. 17. $\mathcal{U}$ is small everywhere and it consistently diminishes with increasing grid density. The relative $\mathcal{U}$ is very small as well, except near the outer boundary, where it gets large simply because $\mathcal{U}$ is extremely small there and thus the ratio that forms rel$\mathcal{U}$ becomes of order unity. In summary, the plots are complimentary and indicate that the constraint is well satisfied.

3. Extraction of the charges

The mass and the tension can be obtained from the asymptotic constants (13) using (14). The constants are extracted by fitting the fields near the outer boundary with analytic expressions of the form (13). It turns out that doing the fitting near r_a is unreliable. Hence, in practice we compute the (averaged along r_a) fields and their r-derivatives, and use this to integrate the fields from r_a to a larger (typically $\sim 10 r_a$) distance. The constants are then extracted from fitting near this boundary. We integrate (6) to get A and C. In order to find B we solve the first order equation obtained after the second derivative $\partial_r^2 B$ in (6) is eliminated with the aid of the constraint G_{zz}. (Using the second order Eq. (6) causes blow-up, see also [18]). Of course in the asymptotic equations we drop the (negligible at large r's) terms containing z-derivatives.

We find that the constant a is essentially robust as it has very little dependence on the details of the integrating-fitting procedure. On the other hand, b is very sensitive to these details and might vary as strong as by 50% when some of them change (see [8,10,18] for related discussions). Therefore the mass, which is essentially determined by a, is obtained accurately, but the tension, which is

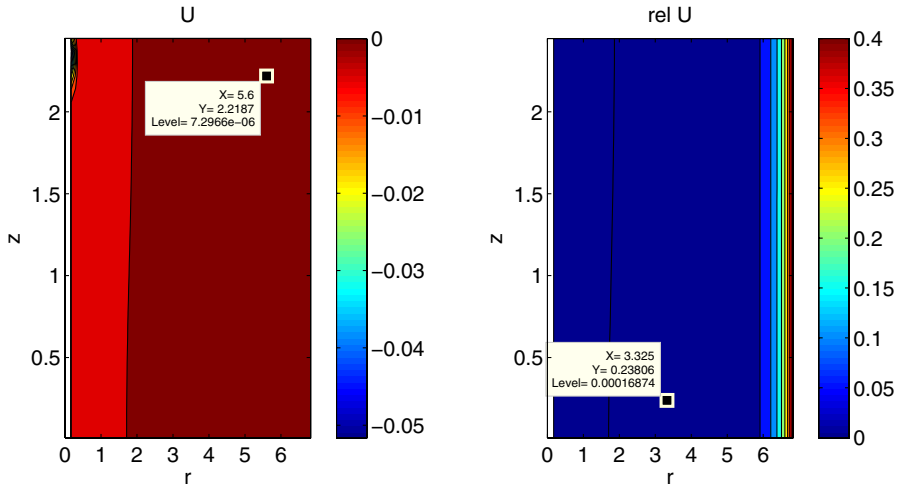

FIG. 17 (color online). The $G_r^z \propto \mathcal{U}$ and rel$\mathcal{U}$ constraints for a strongly nonuniform string ($\lambda \simeq 3.5$) in 6D. The constraint itself is essentially small, with the maximum reached near the horizon. The relative constraint is also very small. The observed growing towards the outer boundary is caused by smallness of $\mathcal{U}$, see the insertions. Both plots are complementary and together they indicate that the constraint is well satisfied.

mainly contributed by b, is not, see (14). In fact we could only confirm that the relative tension is consistently within the range $[0, 1/(D-3)]$ in dimensions $D = 6, 7, 8$.

On the other hand, the local horizon quantities S and T are more accurate since they are measured directly without any additional manipulations that can enhance numerical errors. Hence, it makes sense to try computing the mass by integrating the first law (20) along the solutions branch,

$$m_i(\lambda) = m(0) + \int_0^\lambda T(\lambda')\frac{dS}{d\lambda'}d\lambda'. \tag{B3}$$

We found that the mass computed in this way is close to that obtained from the asymptotic constants. The agreement improves when the numerical resolution increases, see Fig. 5; this indicates the convergence of the numerics. The discrepancy between the mass computed in either way is never above 5%.

Encouraged by this and by the apparent accuracy of Smarr's formula (19), shown in Fig. 6, one might hope to determine the tension without need to invoke the asymptotic integration-fitting procedure. Unfortunately this is not the case. From (19) it follows that the tension is given by the difference of two large numbers,

$$\tau = ((D-3)M - (D-2)ST)/L \tag{B4}$$

each of which becomes larger than τL by more than an order of magnitude for $\lambda \gtrsim 0.1$. One has to know M, S, and T accurately enough to be able to reliably extract $\hat{\tau}$ from (B4). It follows that in our case $\hat{\tau}$ computed from (B4) is very noisy, sometimes with more than 50% scattering. In addition, the accuracy worsens in higher dimensions, partly due to the D-dependent factors in (B4). Consequently, this method does not produce more accurate estimate of τ.

[1] R. Gregory and R. Laflamme, Phys. Rev. Lett. **70**, 2837 (1993).
[2] M. W. Choptuik, L. Lehner, I. Olabarrieta, R. Petryk, F. Pretorius, and H. Villegas, Phys. Rev. D **68**, 044001 (2003).
[3] B. Kol, J. High Energy Phys. 10 (2005) 049.
[4] B. Kol, Phys. Rep. **422**, 119 (2006).
[5] T. Harmark and N. A. Obers, hep-th/0503020.
[6] E. Sorkin, Phys. Rev. Lett. **93**, 031601 (2004).
[7] B. Kol and E. Sorkin, Classical Quantum Gravity **23**, 4563 (2006).
[8] E. Sorkin, B. Kol, and T. Piran, Phys. Rev. D **69**, 064032 (2004).
[9] H. Kudoh and T. Wiseman, Phys. Rev. Lett. **94**, 161102 (2005).
[10] H. Kudoh and T. Wiseman, Prog. Theor. Phys. **111**, 475 (2004).
[11] F. R. Tangherlini, Nuovo Cimento **27**, 636 (1963).
[12] T. Harmark, Phys. Rev. D **69**, 104015 (2004).
[13] D. Gorbonos and B. Kol, J. High Energy Phys. 06 (2004) 053.
[14] D. Gorbonos and B. Kol, Classical Quantum Gravity **22**, 3935 (2005).
[15] Y. Z. Chu, W. D. Goldberger, and I. Z. Rothstein, J. High Energy Phys. 03 (2006) 013.
[16] E. Sorkin (unpublished).
[17] S. S. Gubser, Classical Quantum Gravity **19**, 4825 (2002).
[18] T. Wiseman, Classical Quantum Gravity **20**, 1137 (2003).
[19] B. Kleihaus, J. Kunz, and E. Radu, J. High Energy Phys. 06 (2006) 016.
[20] B. Kol, hep-th/0502033.
[21] S. Hod and T. Piran, Phys. Rev. D **55**, R440 (1997).
[22] C. Gundlach, Phys. Rev. D **55**, 695 (1997).
[23] M. W. Choptuik, Phys. Rev. Lett. **70**, 9 (1993).
[24] E. Sorkin and Y. Oren, Phys. Rev. D **71**, 124005 (2005).
[25] B. Kol and T. Wiseman, Classical Quantum Gravity **20**, 3493 (2003).
[26] T. Wiseman, Phys. Rev. D **65**, 124007 (2002).
[27] B. Kol, E. Sorkin, and T. Piran, Phys. Rev. D **69**, 064031 (2004).
[28] T. Harmark and N. A. Obers, Classical Quantum Gravity **21**, 1709 (2004).
[29] V. Asnin, B. Kol, and M. Smolkin, hep-th/0607129.
[30] B. Kol and E. Sorkin, Classical Quantum Gravity **21**, 4793 (2004).
[31] M. Choptuik and W. G. Unruh, Gen. Relativ. Gravit. **18**, 813 (1986).